FULL PAPER

ADVANCED
HEALTHCARE
MATERIALS

Bioactuators

www.advhealthmat.de

Damage, Healing, and Remodeling in Optogenetic Skeletal Muscle Bioactuators

Ritu Raman, Lauren Grant, Yongbeom Seo, Caroline Cvetkovic, Michael Gapinske, Alexandra Palasz, Howard Dabbous, Hyunjoon Kong, Pablo Perez Pinera, and Rashid Bashir*

A deeper understanding of biological materials and the design principles that govern them, combined with the enabling technology of 3D printing, has given rise to the idea of "building with biology." Using these materials and tools, bio-hybrid robots or bio-bots, which adaptively sense and respond to their environment, can be manufactured. Skeletal muscle bioactuators are developed to power these bio-bots, and an approach is presented to make them dynamically responsive to changing environmental loads and robustly resilient to induced damage. Specifically, since the predominant cause of skeletal muscle loss of function is mechanical damage, the underlying mechanisms of damage are investigated in vitro, and an in vivo inspired healing strategy is developed to counteract this damage. The protocol that is developed yields complete recovery of healthy tissue functionality within two days of damage, setting the stage for a more robust, resilient, and adaptive bioactuator technology than previously demonstrated. Understanding and exploiting the adaptive response behaviors inherent within biological systems in this manner is a crucial step forward in designing bio-hybrid machines that are broadly applicable to grand engineering challenges.

1. Introduction

The functional properties of man-made machines and systems are a direct result of, and therefore limited by, the properties of the materials with which they are built. Biological materials, the most prevalent materials in the natural world, have the ability to sense, process, and respond to a range of environmental signals in real-time. Our deepening understanding of biological materials, and the design principles that govern them, has launched an era of bioinspired and biomimetic design.[1–4] This has driven advances in the field of "smart" materials, where attempts to mimic the complex functionalities demonstrated by biological systems, such as self-assembly and self-healing, have met with significant success.[5–8]

The concurrent rise of advanced manufacturing technologies, such as 3D printing, have enabled ready fabrication of complex geometries from a range of synthetic and biological materials.[9–11] With this tool in hand, we are ideally poised to design and manufacture biointegrated or "bio-hybrid" machines and systems. Such machines, which harness the strengths of both classes of materials, have the potential to achieve more complex functionalities than machines composed of synthetic materials alone.[12,13] This idea has spurred the creation of a range of bio-hybrid robots, or "bio-bots," which have largely focused on proof-of-concept functional demonstrations, such as locomotion driven by biological actuators.[14–19] For example, we have previously presented the first demonstrations of skeletal muscle-powered locomotion in untethered soft robotic devices, controlled by both electrical and optical signals.[18,19]

These bio-bots, formed by coupling tissue engineered skeletal muscle to 3D printed flexible skeletons, are currently capable of directional locomotion and 2D steering in response to noninvasive external signals. Incorporating other types of biological tissue in these machines, such as vascular systems for nutrient transport or neuronal networks for signal processing and higher-level control, promises to expand the range of bio-bot functional behaviors even further.[20–22] Such bio-hybrid systems readily lend themselves toward primary applications in healthcare, such as high-throughput drug testing, targeted drug delivery, and dynamic functional implants. Advanced research in biobatteries and exoskeletons could further expand the scope of such machines to applications in biosecurity and environmental cleanup.

Bridging the gap between the first generation of bio-bots and their eventual real-world applications requires a fundamental understanding of the biological design rules and principles that govern such machines. Any application of these bioactuator

Dr. R. Raman
Department of Mechanical Science and Engineering
Micro and Nano Technology Laboratory
University of Illinois at Urbana-Champaign
Urbana, IL 61801, USA

L. Grant, Dr. C. Cvetkovic, M. Gapinske, A. Palasz,
H. Dabbous, Prof. P. P. Pinera, Prof. R. Bashir
Department of Bioengineering
University of Illinois at Urbana-Champaign
Urbana, IL 61801, USA
E-mail: rbashir@illinois.edu

Dr. Y. Seo, Prof. H. Kong
Department of Chemical and Biomolecular Engineering
University of Illinois at Urbana-Champaign
Urbana, IL 61801, USA

technologies will require them to be dynamically responsive to changing environmental loads and robustly resilient to induced damage. However, there has not been, to our knowledge, any study investigating the response of tissue engineered skeletal muscle to loss-of-function stimuli, or any proposed mechanism for counteracting damage induced in engineered muscle. There is thus a considerable need for understanding the mechanisms of damage in tissue engineered skeletal muscle, and for developing approaches to improve the robustness and resilience of muscle bioactuators. Since the predominant cause of skeletal muscle loss of function is mechanical damage,[23,24] it is essential to investigate the underlying mechanisms of mechanical damage of skeletal muscle in vitro, and to develop in vivo-inspired healing strategies to counteract this damage. Understanding and exploiting the adaptive response behaviors inherent within biological systems is a crucial step forward in designing robust bioactuators that are broadly applicable to engineering grand challenges.

2. Results and Discussion

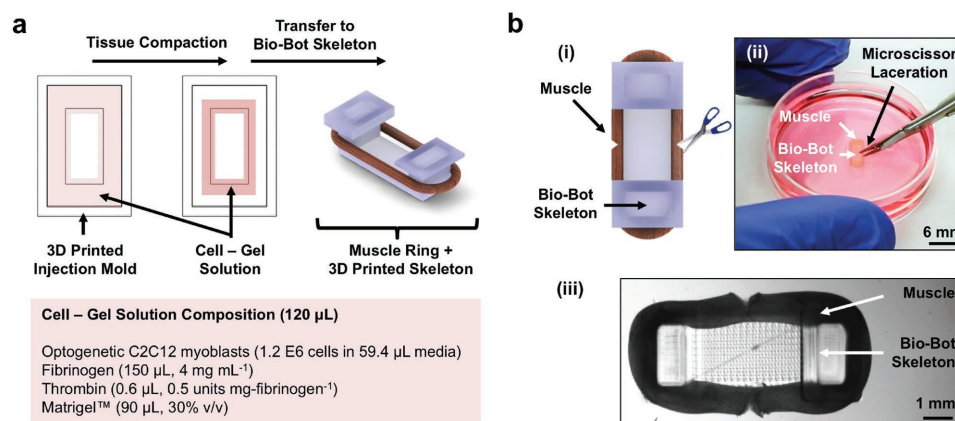### 2.1. Effect of Mechanical Damage on Tissue Engineered Skeletal Muscle

Mechanical damage of muscle in vivo can take many forms, including contusion, overstrain, and laceration.[23] In this study, we chose to investigate muscle functional behavior in response to induced laceration, as this represents the most immediate and severe case of muscle loss of function. When studying the mechanisms of damage in a tissue, the standard practice is to choose the form of damage that most directly impairs its functionality. For example, since fibroblasts play a critical role in wound closure, others have studied damage response in engineered fibroblast microtissues by using knives to lacerate the midsection of the microtissue and observing how the gap is closed by proliferating fibroblasts.[25] The main function of skeletal muscle is controllable, directional force production. Since the primary functional unit of our engineered skeletal muscle is the contractile myotube, and since myotubes are irreversibly

mitotic, we required a mechanism of lacerative damage that would damage or rupture enough myotubes to significantly impair the force production capabilities of the muscle. Moreover, since the longitudinal alignment of myotubes is critical to generating large macro-scale contraction of the tissue, we required a mechanism of lacerative damage that would inhibit longitudinal force transmission across the natural hydrogel matrix which surrounds the muscle cells.

A longitudinal laceration would not satisfy either of these requirements, as it is unlikely to rupture enough myotubes to significantly decrease force output, and the tear in the natural hydrogel matrix could quickly be sealed upon contact between opposite sides of the wound (Figure S1a, Supporting Information) A transverse laceration is much more likely to rupture myotubes and render them incapable of contractility. However, if a transverse laceration is inflicted in the midsection of the tissue, the hydrogel matrix could again be sealed readily upon contact between opposite sides of the wound (Figure S1b, Supporting Information). A transverse laceration at the edges of the engineered muscle tissue would rupture myotubes. It would also reduce alignment of the myotubes in the tissue, and inhibit force transmission across the natural hydrogel matrix. Moreover, opposite sides of the wound cannot readily come into contact to seal the wound (Figure S1c, Supporting Information).

As our aim is to study how tissue engineered skeletal muscle responds to a significant and sustained loss of contractile function, and to develop a healing methodology to counteract this functional loss, we chose transverse laceration of the edges of the engineered tissue as our damage mechanism. While damage to muscle bioactuators in their end-use applications may differ slightly from this approach, the insights that we gain regarding muscle response to inflicted lacerative damage, and mechanisms of recovery, will remain relevant.

Muscle ring bioactuators were formed by injecting a natural hydrogel solution, composed of extracellular matrix mimicking compounds such as Matrigel and fibrin, into a 3D printed mold (**Figure 1**a).[19] Optogenetic C2C12 murine skeletal myoblasts embedded within this natural hydrogel exerted traction forces on this matrix, compacting to form dense 3D muscle tissue ring.

Figure 1. Inducing mechanical damage on tissue engineered skeletal muscle. A) Schematic of muscle ring bioactuator formation in a 3D printed mold. B) Schematic (i) and photographs (ii, iii) of mechanical damage of muscle tissue induced via laceration by sterile microscissors on Day 10 (Movie S1, Supporting Information).

This ring was manually transferred to a 3D printed skeleton, and the resulting device, or "bio-bot," was matured and differentiated using the protocol outlined in Figure S2 (Supporting Information). Given the geometric and material properties of the bio-bot skeleton, which was composed of the biocompatible hydrogel poly (ethylene glycol) diacrylate (PEGDA M_w 700 g mol^{-1}), contractile forces exerted by the muscle ring bioactuators in response to a blue-light stimulus (470 nm) could be readily calculated from the resultant displacement of the skeleton (Figure S3a,b, Supporting Information).[19,26] This provided us with a simple and efficient mesoscale model with which to investigate the effects of mechanical damage on skeletal muscle in vitro.

Mechanical damage was induced via manual laceration of the muscle ring using sterile microscissors on Day 10 (Figure 1b, Movie S1, Supporting Information). Muscle tissue cross-sectional area, represented as a percentage of its predamage value and measured from top-view images, decreased significantly 24 h postdamage and reached a steady-state thereafter for damages ranging from 40% to 60% original cross section (**Figure 2**a). This trend was preserved for smaller-scale damages above 60% original cross section. Larger damages (below 40% original cross section) led to more rapid reduction in cross-sectional area 24 h postdamage and continuing decreases in area thereafter (Figure S4a,b, Supporting Information). The fraction of bioactuators that completely ruptured by Day 17 was 50% for muscle damage below 40% of the original cross section, 20% for 40%–60% of original cross section, and 0% for damaged muscle above 60% original cross section.

Postdamage cross-sectional area demonstrated a linear correlation with the percentage loss in passive tension exerted by the muscle (Figure 2b). Damaged muscle rings in the range of 45%–55% original cross section, which represented significant loss of function without a resultant instability in the remaining undamaged tissue, were used for all future experiments. Cellular viability in these muscle rings demonstrated a significant drop to 91% ± 3% of the healthy tissue value 1 h postdamage, further reducing to 86% ± 4% one week postdamage (Figure 2c). However, the viability decrease between Day 10 and Day 17 was not significant, indicating that cellular viability and functionality in the undamaged portion of muscle tissue did not continue to decrease after induced mechanical laceration.

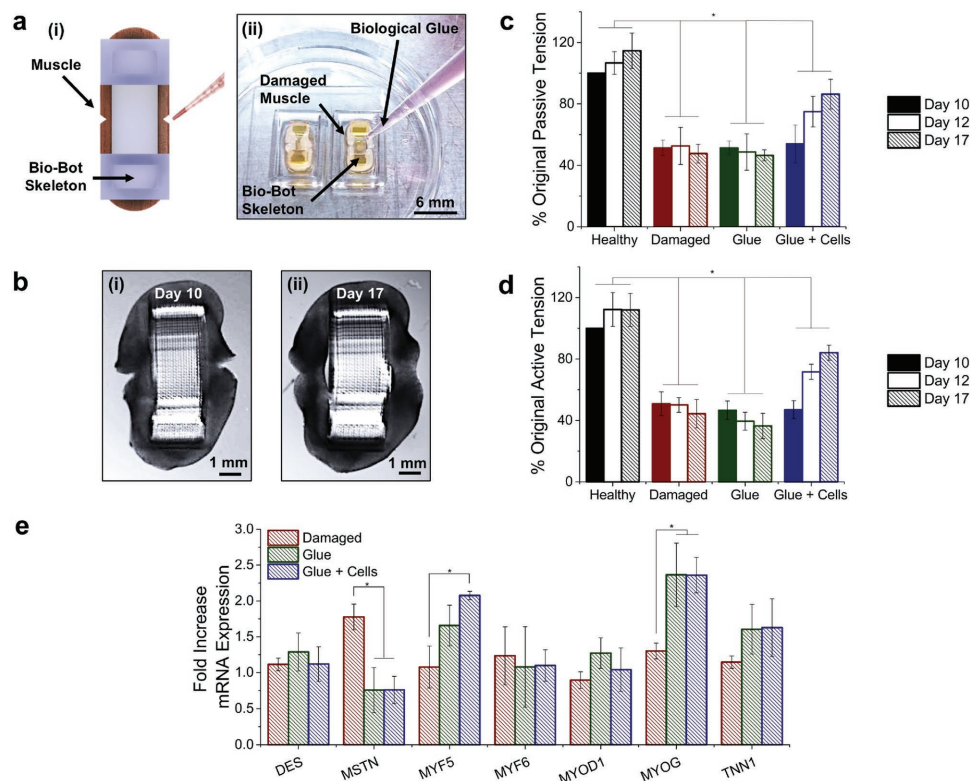## 2.2. Repairing Mechanical Damage in Tissue Engineered Skeletal Muscle

2.2.1. Sealing Lacerative Damage with a Biological Glue

To obtain further evidence that the differentiated myotubes in the lacerated section of the tissue had undergone irreversible damage, we sealed the tear in the muscle using an acellular biological glue of the same composition as the surrounding muscle matrix (**Figure 3**a,b). Passive and active tension generated by muscle rings healed with this glue were not significantly different from those generated by damaged muscle rings (Figure 3c,d), indicating that the reduction in force production was not merely a result of inefficient force transmission across the matrix. Sealing the wound with the glue did, however, have the positive effect of reducing complete rupture of muscle rings from 20% to 0%, as compared to damaged muscle rings one week postdamage.

Since myotubes are irreversibly mitotic,[23] it is perhaps unsurprising that healing the lacerative damage with a biological glue did not result in improved force production. In vivo, skeletal muscle damage is healed via satellite cells which migrate to the site of injury, proliferate to form myoblasts, and differentiate into contractile myotubes.[24] To mimic this procedure in vitro, we incorporated undifferentiated optogenetic C2C12 myoblasts within the biological glue used to seal muscle damage. This resulted in significant increases in passive and active tension one week postdamage, on the order of 86% ± 10% (1230 ± 140 µN) and 84% ± 5% (138 ± 8.1 µN) of predamage values, respectively (Figure 3c,d). A comparison of the expression levels of a range of muscle specific proteins (Figure 3e) revealed that damaged muscle rings that did not undergo any healing intervention expressed significantly higher levels of *MSTN*, an inhibitory factor that prevents muscle growth and differentiation.[27] Muscle rings healed with biological glue, both with and without embedded myoblasts, expressed significantly higher levels of *MYOG*, a factor that helps coordinate muscle growth and repair.[28] Only muscle rings healed with biological glue containing myoblasts showed significant increases in the expression of *MYF5*, a protein that performs an important role in muscle regenerative growth and differentiation.[29] While these results were a promising indication of the regenerative
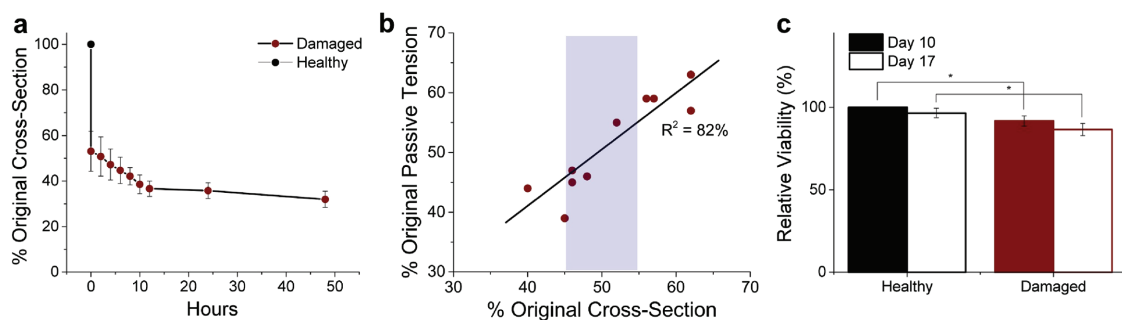
Figure 2. Effect of mechanical damage on tissue engineered skeletal muscle. A) Wound closure over time, measured via top-view images of muscle tissue cross-sectional area ($n = 3$). B) Reduction in muscle passive tension force production is directly correlated to degree of damage inflicted by laceration. Damaged muscle rings in the shaded portion of this graph (45%–55% original cross section) were used for all the data shown in this study. C) Comparison of viability between healthy muscle tissue and damaged muscle tissue 1 h postdamage (Day 10) and one week postdamage (Day 17) shows a significant reduction of viability in damaged tissue ($P < 0.05$, $n = 3$, one-way ANOVA, post hoc Tukey test).

**ADVANCED
SCIENCE NEWS**
www.advancedsciencenews.com

**ADVANCED
HEALTHCARE
MATERIALS**
www.advhealthmat.de

Figure 3. Repairing mechanical damage in tissue engineered skeletal muscle. A) Schematic (i) and photograph (ii) of sealing laceration in damaged muscle using a biological glue. Bio-bots are placed within a 3D printed PEGDA holder to keep them in place during the wound sealing process. B) Top-view images of muscle tissue immediately postdamage (i) and one week postwound sealing using a biological glue (ii). C) Plot of passive tension for damaged and healed muscle tissue, represented as a percentage of passive tension generated by healthy muscle tissue on Day 10. Sealing the damage with a biological glue does not significantly affect force production, but healing the damage with a biological glue containing undifferentiated myoblasts yields significant increases in force production ($P < 0.05$, $n = 3$, one-way ANOVA, post hoc Tukey test). D) Plot of active tension for damaged and healed muscle tissue, represented as a percentage of active tension generated by healthy muscle tissue on Day 10. Sealing the damage with a biological glue does not significantly affect force production, but healing the damage with a biological glue containing undifferentiated myoblasts yields significant increases in force production ($P < 0.05$, $n = 3$, one-way ANOVA, post hoc Tukey test). E) Quantitative PCR is used to compute fold increase in protein expression across three groups (damaged, biological glue, and biological glue containing myoblasts) as compared to a control (undamaged). Proteins analyzed include: *DES, MSTN, MYF5, MYF6, MYOD1, MYOG,* and *TNN1*.

effects of the biological glue containing myoblasts, the values of force production generated by muscle healed with this method were still significantly lower than those for healthy tissue. This indicated a need to develop a strategy for more accelerated and complete recovery of force production.

2.2.2. Remodeling Tissue Engineered Skeletal Muscle

Muscle force production in vivo can be improved via exercise.[24,30] Several studies of tissue engineered skeletal muscle have shown that force production can also be improved in vitro through "exercise" in the form of a static mechanical stimulus, dynamic mechanical stimulus, or dynamic electrical stimulus.[21,26,31,32] We have previously shown that the functional performance of optogenetic tissue engineered skeletal muscle can likewise be tuned through dynamic optical stimulation during differentiation.[19] While this noninvasive approach of regulating force production has been proven, it has yet to be empirically optimized.

Our engineered muscle tissue demonstrated physiological force-frequency response behavior, where an increase in stimulation frequency corresponded to a reduction in the dynamic range of active tension force produced (Figure S5a, Supporting Information). Paced force production was tested from 1 to 10 Hz, with tetanus observed in the 8–10 Hz range. Since a stimulation frequency of 1 Hz resulted in the greatest contractile strain imposed on the muscle, this frequency was chosen to optimize the optical exercise training protocol.

To investigate the possibility that an optical exercise stimulation protocol could be used to accelerate the recovery of force production in healed muscle rings, we optically stimulated muscle rings at 1 Hz for timescales ranging from 15–60 min using a 470 nm LED (**Figure 4**a, Figure S5b, Supporting Information). Passive and active tension force production improved in response to exercise training, with significant increases observed up to 30 min of stimulation (Figure 4b, Figure S5c, Supporting Information). Muscle rings subjected to the 30 minute optical stimulation regimen produced passive tension forces of 2250 ± 120 µN and active tension forces of
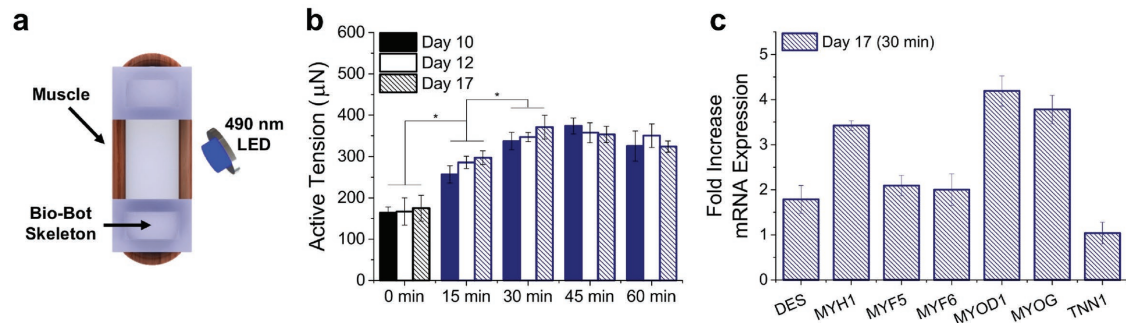
Figure 4. Remodeling tissue engineered skeletal muscle. A) Schematic of 470 nm blue-light stimulation (1.9 mW mm^{-2} power density) of tissue engineered optogenetic skeletal muscle. B) Active tension force generated by skeletal muscle is regulated by daily optical stimulation exercise training (0–60 min at 37 °C), with significant increases observed up to 30 min stimulation. Stimulation for longer time periods does not result in significant increases in force production. C) Quantitative PCR is used to compute fold increase in protein expression for the optimized exercise treatment groups (30 min) as compared to a control (0 min). Proteins analyzed include: *DES, MYH1, MYF5, MYF6, MYOD1, MYOG,* and *TNN1.*

371 ± 29 µN on Day 17. Stimulation for longer time periods did not result in further significant increases in force production. An analysis of mRNA expression in muscle rings exercised for 30 min showed significant increases in the expression of factors that play key roles in myogenesis and differentiation (*DES, MYH1, MYF5, MYF6, MYOD1, MYOG,* and *TNN1*), as compared to control muscle rings that did not undergo exercise (Figure 4c).[33]

2.2.3. Accomplishing Complete Recovery of Muscle Force Production Postdamage

Having optimized the optical stimulation protocol for improving muscle force production, we investigated the effect of integrating an exercise regimen with the healing approach outlined in Figure 3. Specifically, we compared three groups on their ability to recover the force produced by undamaged muscle rings: Group 1 contained optogenetic muscle rings healed with optogenetic myoblasts, Group 2 contained optogenetic muscle rings healed with wild type C2C12 myoblasts (myoblasts that have not been engineered to respond to blue light), and Group 3 contained muscle rings composed of wild type C2C12 myotubes healed with optogenetic C2C12 myoblasts (**Figure 5**a).

Active tension forces produced by healed muscle rings were tested via electrical stimulation, which activates contraction in both wild type and optogenetic C2C12 myotubes.

Muscle rings in Groups 2 and 3 demonstrated significant increases in force production when measured 2 d and one week posthealing (Figure 5b). However, they were unable to reproduce the contractile forces generated by healthy muscle tissue. By contrast, muscle rings in Group 1 produced active tension forces comparable to those produced by healthy undamaged tissue one week postdamage (Figure 5c). Group 1 muscle rings generated active tension forces of 169 ± 19 µN, when stimulated at 1 Hz on Day 17, similar to healthy undamaged tissue which produced active tension forces of 175 ± 31 µN.

In all three groups, the addition of undifferentiated myoblasts during the healing process served to counteract muscle loss-of-function by upregulating expression of *MYOG* and *MYF5* and downregulating expression of *MSTN*, as shown in Figure 3e. Optically exercising exclusively the undamaged portion of the muscle ring (Group 2) or the new tissue added during the healing process (Group 3) served to upregulate the expression of *DES, MYH1, MYF5, MYF6, MYOD1, MYOG,* and *TNN1* only in those portions of the tissue, as shown in Figure 4c. Group 1 muscle rings experienced the synergistic effects of the addition of new cells, exercise of the undamaged
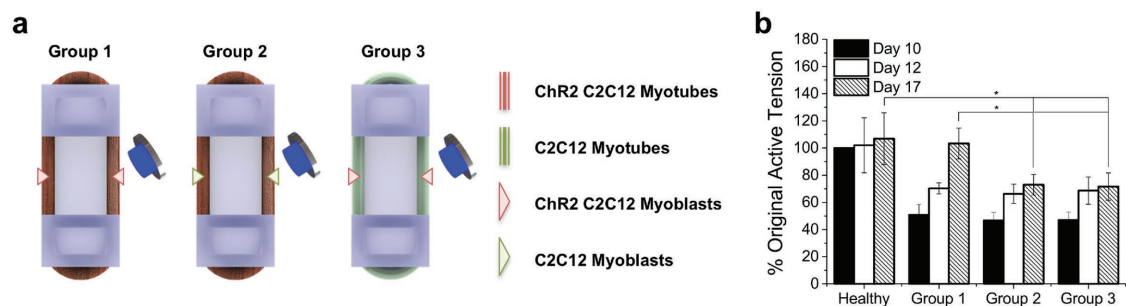
Figure 5. Recovering healthy tissue functionality in damaged skeletal muscle. A) Schematic of three test groups designed to test the efficacy of exercising the myotubes in the muscle ring and the myoblasts in the biological glue separately and together. B) Plot of active tension for damaged and healed muscle tissue, represented as a percentage of active tension generated by healthy muscle tissue on Day 10. Muscle rings in which both the undamaged myotubes and myoblasts added during healing were exercised for 30 min showed the most significant increases in force production.

portion of the muscle, and exercise of the tissue added during the healing process. This coordinated downregulation of *MSTN* and tissue-wide upregulation of *DES, MYH1, MYF5, MYF6, MYOD1, MYOG,* and *TNN1* led to significant increases in force production over both damaged tissue and healed muscle from experimental Groups 2 and 3. This indicates that exercise stimulation of both the undamaged and newly formed tissue created during the healing process is required to fully regain force production at predamage levels.

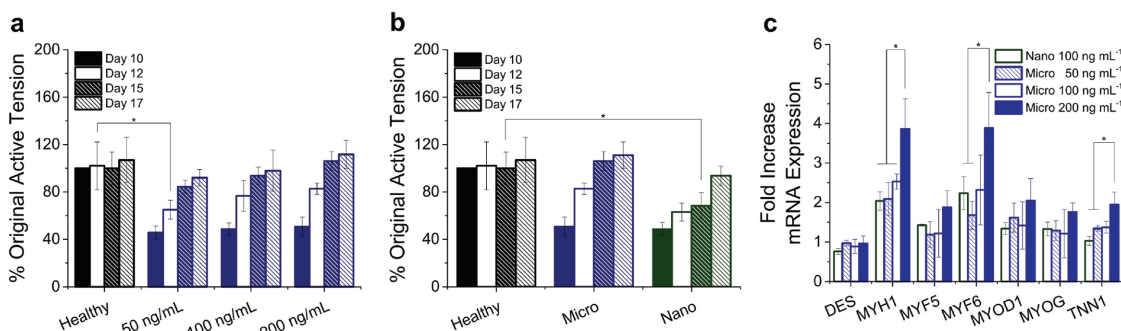### 2.2.4. Accelerating Wound Healing Response in Tissue Engineered Skeletal Muscle

While regaining predamage functionality is a significant accomplishment, accelerating the healing process to recover functional performance over a shorter time period could prove to be of great value in real-world bioactuator applications. The hypertrophic effect of human insulin-like growth factor (IGF-1) on skeletal muscle tissue has been well established in vivo and in vitro.[34,35] We have previously shown that incorporating IGF-1 at a concentration of 50 ng mL^{-1} into our muscle differentiation media results in significant improvements in muscle force production, as well as accelerated maturation of muscle tissue to a contractile state.[26] Prior studies have shown that localized release of growth factors can be an effective method of enhancing tissue regeneration.[36] To test the effects of a concentrated and sustained local release of IGF-1 near the site of damage, we incorporated IGF-loaded poly (lactic-*co*-glycolic acid) (PLGA) microparticles (3.1 ± 1 µm in diameter) into the biological glue containing undifferentiated optogenetic myoblasts (**Figure 6**a, and Figures S6 and S7a,b, Supporting Information).

The biological glue containing microparticles was prepared at concentrations of 50, 100, and 200 ng mL^{-1} IGF-1 and injected at the site of damage. Muscle ring active tension was measured 1 h posthealing (Day 10) and measured every day

following up to one week postdamage (Day 17). Muscle rings were also subjected to 30 min of daily optical stimulation at 1 Hz during this period. In all three cases, muscle rings produced active tension forces on the order of healthy tissue values by Day 15 (Figure 6b). Furthermore, muscle rings treated with the higher concentrations of 100 and 200 ng mL^{-1} IGF-1 produced active tension forces of 126 ± 21 µN and 136 ± 7.7 µN respectively, on the order of healthy tissue values, by Day 12. By contrast, the Group 1 muscle rings healed without microparticles (Figure 5c) did not regain predamage force production values until Day 17. This indicated that concentrated release of IGF-1 near the site of damage served to accelerate the rate of wound healing in muscle rings.

Healing response to a biological glue containing IGF-loaded nanoparticles (220 ± 60 nm in diameter) at a concentration of 100 ng mL^{-1} IGF-1 was also tested, revealing that muscle rings did not regain pre-damage values of force production until one-week posthealing (Figure 6b, Figure S6c,d, Supporting Information), similar to the Group 1 muscle rings shown in Figure 5. The difference in healing rates between the microparticle-containing glue and the nanoparticle-containing glue could be attributed to diffusion of the nanoparticles out of the tissue. Microparticles were similar in size to single C2C12 myoblasts (8–10 µm diameter), as compared to the nanoparticles, which were significantly smaller. As a result, microparticles were more likely to be trapped within the 3D muscle matrix, resulting in sustained local release of IGF-1 at the damage site.

Expression levels of a range of muscle specific proteins in muscle rings healed with IGF-loaded micro- and nanoparticles are shown in Figure 6c, represented as fold increases over muscle rings healed with cells and exercise alone. The expression levels of *DES, MYF5, MYOD1,* and *MYOG* on Day 17 are not significantly different across experimental groups. However, muscle rings treated with the highest concentration of IGF-1 (200 ng mL^{-1}) expressed *MYH1*, the protein that forms the muscle contractile apparatus and converts chemical energy from ATP hydrolysis to mechanical energy,[37] at significantly

Figure 6. Accelerating wound healing response in tissue engineered skeletal muscle. A) Plot of active tension for damaged and healed muscle tissue, represented as a percentage of active tension generated by healthy muscle tissue on Day 10. Incorporating IGF-loaded microparticles in the biological glue accelerated wound healing response for all three concentrations tested, with all cases resulting in force production values on the order of healthy tissue by Day 15. Higher concentrations of IGF-1 (100 and 200 ng mL^{-1}) resulted in faster recovery times, with healthy tissue functionality gained within two days of damage and healing. B) Plot of active tension for damaged and healed muscle tissue, represented as a percentage of active tension generated by healthy muscle tissue on Day 10. The incorporation of nanoparticles in the biological glue did not accelerate wound healing response time, with healthy tissue levels of functionality only regained one week postfab, as in the Group 1 muscle presented in Figure 3. C) Quantitative PCR is used to compute fold increase in protein expression for the IGF-loaded micro- and nanoparticle treatment groups (exercised 30 min daily) as compared to a control (healed with biological glue containing cells and no microparticles, exercised 30 min daily). Proteins analyzed include: *DES, MYH1, MYF5, MYF6, MYOD1, MYOG,* and *TNN1*.

ADVANCED
SCIENCE NEWS
www.advancedsciencenews.com

ADVANCED
HEALTHCARE
MATERIALS
www.advhealthmat.de

higher levels than all other experimental groups. Furthermore, they expressed *MYF6* and *TNN1*, a regulatory protein that controls myosin-actin binding,[38] at significantly higher levels than rings treated with microparticles at 50 ng mL^{-1} and nanoparticles at 100 ng mL^{-1}. Muscle rings in the 200 ng mL^{-1} IGF-1 treatment group did produce larger active tension forces (184 ± 20 µN on Day 17) in response to optical stimulation at 1 Hz (Figure 6a), but these increases were not significantly greater than those in other test groups.

It is interesting to note that while the muscle rings in the damaged and healed groups were exercised daily for 30 min, they did not produce significantly greater values of active tension force than the unexercised healthy tissue. This contrasts with the data shown in Figure 4b, where undamaged muscle rings that were exercised demonstrated, on average, a 210% increase in force production by Day 17. This indicates that even though healed muscle rings rapidly recover force production on the order of healthy unexercised tissue, there is still a lasting effect of damage on the skeletal muscle bioactuators that affects muscle performance one week postdamage. Future studies could further investigate the longer term mechanisms underlying muscle remodeling postdamage.

2.2.5. Skeletal Muscle Tissue Architecture Postdamage and Healing

To visualize muscle architecture in the muscle rings healed with microparticles (200 ng mL^{-1} IGF-1), we imaged immunostained muscle rings in a fluorescence confocal microscope (**Figure 7**). Muscle rings fixed and stained 1 h postdamage, and imaged at the damage site (Figure 7a), showed cell nuclei (DAPI, blue) throughout the damage site. The original muscle

Figure 7. Muscle tissue architecture postdamage and healing. Confocal images of damaged and healed muscle tissue on A) Day 10 and B,C) Day 17. Original muscle tissue is represented by red, new muscle tissue is dyed green, cell nuclei are blue (DAPI), and myosin is marked by a yellow dye. Muscle cells added during the wound sealing process spread across the existing tissue and develop mature functional myotubes during the healing process.

tissue (red) occupies the inner undamaged portion of the muscle ring, while the outer damaged portion is composed primarily of myoblasts (green) added during the healing process. Since these added cells are undifferentiated, myosin (yellow) is only visible in the inner portion of the muscle ring, which is composed of mature muscle tissue.

By Day 17, the myoblasts added during the healing intervention spread across the damage site (Figure 7b) and are not physically separated from the original undamaged portion of the muscle tissue (Figure 7c). Myosin is expressed uniformly in the original and new muscle tissue, corroborating the recovery in force production observed empirically. This indicates that the healing strategy we have developed mimics the process of healing in vivo, where the myoblasts in the biological glue act as satellite cells that counteract irreversible mitotic damage in lacerated myotubes.
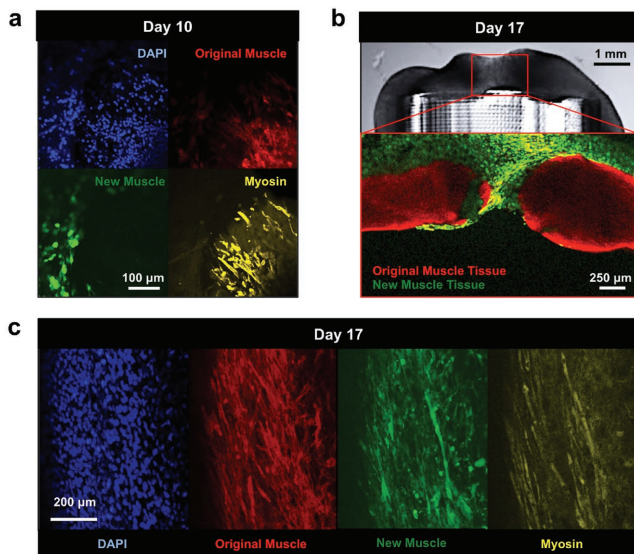
3. Conclusion

We have developed a mesoscale model for studying skeletal muscle physiology in vitro and used it to create an efficient and effective healing strategy to counteract mechanical damage in engineered skeletal muscle. A similar approach could be used to study skeletal muscle pathologies and test the effects of various drugs on both muscle architecture and functional performance. A deepening understanding of muscle healing in vitro could also be applied to develop optimized healing methodologies for volumetric muscle loss injuries in vivo.[39,40]

In addition to these more immediate applications in healthcare, this study presents a significant step forward in creating a more robust, resilient, and adaptive bioactuator technology for other engineering challenges. While recent advances in developing self-healing synthetic materials have met with significant success, they have yet to demonstrate, to our knowledge, complete recovery of pre-damage functionality in such materials.[5,41–43] Furthermore, these studies have focused on healing static materials, using mechanical strength as a measure of recovery, rather than on healing dynamic materials capable of controllable actuation. Considering that skeletal muscle can produce larger strains and forces from a more compact volume than any synthetic actuator to date,[44] and that biological materials have the ability to dynamically adapt to a range of environmental cues, there is a strong motivation to develop robust skeletal muscle bioactuators for bio-hybrid machines and systems.

We have developed a skeletal muscle bioactuator that can completely recover from large volume damages within two days postdamage, when treated with an optimized healing strategy that combines new myoblasts, extracellular matrix proteins, exercise, and sustained local release of insulin-like growth factor. Future work could further increase the degree of autonomy, or "self-healing" demonstrated by these actuators, by incorporating vascular-like networks within the muscle rings which release myoblasts or biochemical factors upon induced damage.

By coupling the complex and adaptive functional capabilities of biological tissues with the increasingly vast array of synthetic materials, we have the opportunity to create bio-hybrid machines and systems that have broad applicability toward

**ADVANCED
SCIENCE NEWS**

www.advancedsciencenews.com

**ADVANCED
HEALTHCARE
MATERIALS**

www.advhealthmat.de

real-world challenges in healthcare, defense, and the environment.[12,19,26,45] This study advances the goal of understanding and exploiting the fundamental design rules and principles that govern "building with biology," and sets the stage for forward-engineering the next generation of bio-hybrid machines and systems.

4. Experimental Section

Stereolithographic 3D Printing of Muscle Ring Injection Molds and Bio-Bot Skeletons: An adapted form of a commercially available stereolithographic 3D printer (SLA 250/50, 3D Systems) was used to manufacture muscle ring injection molds and bio-bot skeletons as previously described.[19] Molds were printed using a 20% (w/v) PEGDA resin of molecular weight 1000 g mol^{-1} (Polysciences) and skeletons were printed using a 20% (v/v) PEGDA resin of molecular weight 700 g mol^{-1} (Sigma-Aldrich). Fabricated parts were sterilized prior to cell culture by immersion in 70% (v/v) ethanol for 1 h, followed by immersion in phosphate buffered saline (PBS) for 1 h.

Muscle Ring Seeding and Differentiation: C2C12 murine myoblasts transduced to express a mutant variant of the 470 nm blue-light sensitive cation channel, Channelrhodopsin-2 (ChR2[H134R])[46] were cultured in growth medium (GM) consisting of Dulbecco's Modified Eagle Medium with L-glutamine and sodium pyruvate (DMEM, Corning) and supplemented with 10% (v/v) fetal bovine serum (FBS, Lonza), 1% (v/v) L-glutamine (Cellgro Mediatech), and 1% (v/v) penicillin-streptomycin (Cellgro Mediatech). Muscle cells were trypsinized and resuspended (at a concentration of 1E7 cells mL^{-1}) in a natural hydrogel matrix consisting of 30% (v/v) Matrigel (BD Biosciences), 4 mg mL^{-1} fibrinogen (Sigma-Aldrich), and 0.5 units mg-fibrinogen^{-1} thrombin (Sigma-Aldrich). This suspension was pipetted into the 3D printed injection molds and incubated for 1 h at 37 °C prior to being immersed in GM supplemented with 1 mg mL^{-1} aminocaproic acid (ACA, Sigma-Aldrich) (GM+). On Day 3 postseeding, muscle rings were transferred to differentiation medium (DM) consisting of DMEM supplemented with 10% (v/v) heat inactivated horse serum (HS, Lonza), 1% (v/v) L-glutamine (Cellgro Mediatech), and 1% (v/v) penicillin-streptomycin (Cellgro Mediatech). This DM was further supplemented with 1 mg mL^{-1} ACA and 50 ng mL^{-1} human insulin-like growth factor-1 (IGF-1, Sigma Aldrich) (DM++). Muscles started demonstrated controllable twitch response to optical stimulation at Day 7 postseeding.

Damage and Healing of Muscle Rings with Biological Glue: Muscle damage was induced via laceration with sterile microscissors (Ted Pella). The biological glue used to heal the tear in the muscle was composed of the same cell/hydrogel matrix used during the muscle ring seeding process. For muscle rings healed with IGF-loaded micro- and nanoparticles, the particles were mixed thoroughly into the cell/hydrogel solutions at concentrations of 50, 100, and 200 ng mL^{-1} IGF-1. For muscle rings healed for confocal imaging, cells were stained with a green dye (CMFDA, Thermo Fisher Scientific) as per the manufacturer's instructions.

Muscle Optical and Electrical Stimulation and Force Measurement: Muscle rings were stimulated optically using a 470 nm blue-light LED connected to a function generator producing pulse trains of specified frequencies (1–4 Hz) and pulse widths (50 ms). Muscle rings were stimulated electrically in serum-free media using a custom-built apparatus.[18] Passive tension force was measured by correlating bio-bot skeleton beam deflection to the force generated by the engineered muscle, using a formula derived from Euler–Bernoulli beam bending theory, as previously described (Figure S2b, Supporting Information).[18] Active tension force was similarly calculated by correlating skeleton deflection to muscle contractile force production using a formula derived from Kelvin–Voigt viscoelasticity theory, as previously described (Figure S2c, Supporting Information).[18]

Synthesis of IGF-Loaded Microparticles and Nanoparticles: IGF-containing PLGA micro- and nanoparticles were prepared via a double emulsification method ($W_1/O/W_2$). 100 µg of IGF-1 (Sigma Aldrich)

was dissolved in 100 mL of 10×10^{-3} M HCl solution for preparing a stock solution of 1 mg mL^{-1}. The water phase 1 (W_1) was prepared by adding 10 µL of IGF-1 stock solution into 200 µL cell-culture grade water (Corning). This was then added to an organic phase (O) consisting of dichloromethane (DCM, 1.5 mL) containing 20 mg PLGA (LACTEL, lactic:glycolic = 50:50, M_w 6000–10 000 g mol^{-1}, DURECT) followed by vortexing (microparticle) or sonication (nanoparticle) for 3 min to form a W_1/O emulsion. This primary emulsion (W_1/O) was then transferred to 12 mL of 1% (w/v) aqueous PVA solution (W_2), and the mixture was vortexed (microparticle) or sonicated (nanoparticle) again for 3 min to form the secondary emulsion ($W_1/O/W_2$). This mixture was continuously stirred for 6 h. The resulting micro- and nanoparticles were collected via centrifugation at 2000 and 12 000 rpm for 10 min and washed with cell-culture grade water, respectively. This purification process was repeated three times. After this purification step, IGF-PLGA particles were lyophilized and stored at −20 °C. Microparticles were imaged with an optical microscope (Leica DML) and the size distribution was obtained via image analysis with ImageJ software (NIH). Nanoparticles were imaged using a transmission electron microscope (JEOL 2100 TEM) with an accelerating voltage of 200 kV. Nanoparticle size distribution was determined in DI water at room temperature with dynamic light scattering (Malvern Zetasizer Nano ZS).

Analysis of Protein Expression via Quantitative PCR: Muscle rings were flash-frozen in liquid nitrogen. The rings were homogenized by vortexing in RLT buffer (Qiagen) with 10 uL mL^{-1} B-mercaptoethanol, and centrifuged using the QIAshredder (Qiagen) column. RNA was extracted using the RNeasy Plus RNA isolation kit (Qiagen) according to the manufacturer's instructions. cDNA synthesis was done using the qScript cDNA SuperMix (Quanta Biosciences) from 100 ng of RNA and reactions were performed as directed by the supplier. For RT-qPCR, SsoFast EvaGreen Supermix (Bio-Rad) was added to cDNA and primers targeting the genes of interest and GAPDH (Table S1, Supporting Information). The cycling parameters were 30 s at 95 °C, and 40 cycles of 5 s at 95 °C and 20 s at 55 °C, followed by melt-curve analysis of the product using a CFX Connect Real-Time System (Bio-Rad). Ct values were used to calculate changes in expression level, relative to GAPDH and control samples by the 2 -ΔΔCt method. Reaction efficiencies over the appropriate dynamic range were calculated to ensure linearity of the standard curve.

Immunohistochemical Staining and Confocal Imaging of Muscle Rings: Muscle rings were rinsed in PBS and fixed in 4% (v/v) paraformaldehyde (EMD Chemicals) for 30 min, prior to permeabilization with 0.2% (v/v) Triton X-100 (Sigma-Aldrich) for 10 min and immersion in Image-iT FX Signal Enhancer blocking solution (Invitrogen). Muscle rings were incubated in mouse antimyosin heavy chain (MF-20, Developmental Studies Hybridoma Bank, The University of Iowa Department of Biology) at a 1:300 (v/v) dilution in Image-iT FX blockin solution for 8 h at 4 °C on a shaker. They were then incubated in anti-mouse IgG secondary antibody (Alexa Fluor 647) at a 1:300 (v/v) dilution in blocking solution for 12 h at 4 °C. They were finally incubated in 4′,6-diamindino-2-phenylindole (DAPI, Sigma-Aldrich) at a 1:5000 (v/v) dilution in sterile deionized water for 10 min. Stained muscle rings were placed onto a glass-bottom petri dish (MatTek) and covered in a warm agarose gel prior to imaging with a fluorescence confocal microscope (LSM 710, Zeiss).

Supporting Information

Supporting Information is available from the Wiley Online Library or from the author.

Acknowledgements

Conflict of Interest

The authors declare no conflict of interest.

Keywords

[1] C. Sanchez, H. Arribart, M. M. G. Guille, *Nat. Mater.* **2005**, *4*, 277.
[2] F. Xia, L. Jiang, *Adv. Mater.* **2008**, *20*, 2842.
[3] J. Aizenberg, P. Fratzl, *Adv. Funct. Mater.* **2013**, *23*, 4398.
[4] G. M. Whitesides, *Interface Focus* **2015**, *5*, 20150031.
[5] S. R. White, N. R. Sottos, P. H. Geubelle, J. S. Moore, M. R. Kessler, S. R. Sriram, E. N. Brown, S. Viswanathan, *Nature* **2001**, *409*, 1804.
[6] C. E. Diesendruck, N. R. Sottos, J. S. Moore, S. R. White, *Angew. Rev.* **2015**, *54*, 2.
[7] G. M. Whitesides, B. Grzybowski, *Science* **2002**, *295*, 2418.
[8] M. A. McEvoy, N. Correll, R. Summary, *Science* **2015**, *347*, 1261689.
[9] S. V. Murphy, A. Atala, *Nat. Biotechnol.* **2014**, *32*, 773.
[10] F. P. W. Melchels, J. Feijen, D. W. Grijpma, *Biomaterials* **2010**, *31*, 6121.
[11] R. Raman, R. Bashir, *Stereolithographic 3D Bioprinting for Biomedical Applications*, Elsevier Inc., The Netherlands, **2015**.
[12] R. D. Kamm, R. Bashir, *Ann. Biomed. Eng.* **2014**, *42*, 445.
[13] A. W. Feinberg, *Annu. Rev. Biomed. Eng.* **2015**, *17*, 243.
[14] A. W. Feinberg, A. Feigel, S. S. Shevkoplyas, S. Sheehy, G. M. Whitesides, K. K. Parker, *Science* **2007**, *317*, 1366.
[15] J. C. Nawroth, H. Lee, A. W. Feinberg, C. M. Ripplinger, M. L. McCain, A. Grosberg, J. O. Dabiri, K. K. Parker, *Nat. Biotechnol.* **2012**, *30*, 792.
[16] V. Chan, K. Park, M. B. Collens, H. Kong, T. a. Saif, R. Bashir, *Sci. Rep.* **2012**, *2*, 857.
[17] B. J. Williams, S. V. Anand, J. Rajagopalan, M. T. a. Saif, *Nat. Commun.* **2014**, *5*, 1.
[18] C. Cvetkovic, R. Raman, V. Chan, B. J. Williams, M. Tolish, P. Bajaj, *Proc. Natl. Acad. Sci. USA* **2014**, *111*, 10125.
[19] R. Raman, C. Cvetkovic, S. G. M. Uzel, R. J. Platt, P. Sengupta, R. D. Kamm, *Proc. Natl. Acad. Sci. USA* **2016**, *113*, 3497.
[20] L. G. Griffith, G. Naughton, *Science* **2002**, *295*, 1009.
[21] R. M. Duffy, A. W. Feinberg, *Wiley Interdiscip. Rev.: Nanomed. Nanobiotechnol.* **2014**, *6*, 178.
[22] V. Chan, H. H. Asada, R. Bashir, *Lab Chip* **2014**, *14*, 653.
[23] T. A. H. Järvinen, T. L. N. Järvinen, M. Kääriäinen, *Am. J. Sports Med.* **2005**, *33*, 745.
[24] R. Sambasivan, S. Tajbakhsh, *Results Probl. Cell Differ.* **2015**, *56*, 191.
[25] M. Selman Sakar, J. Eyckmans, R. Pieters, D. Eberli, B. J. Nelson, C. S. Chen, *Nat. Commun.* **2016**, *7*, 1.
[26] C. Cvetkovic, R. Raman, V. Chan, B. J. Williams, M. Tolish, P. Bajaj, M. S. Sakar, H. H. Asada, M. T. A. Saif, R. Bashir, *Proc. Natl. Acad. Sci. USA* **2014**, *111*, 10125.
[27] S. B. P. Chargé, M. a. Rudnicki, *Physiol. Rev.* **2004**, *84*, 209.
[28] S. Dedieu, G. Mazères, P. Cottin, J. J. Brustis, *Int. J. Dev. Biol.* **2002**, *46*, 235.
[29] B. Gayraud-Morel, F. Chrétien, P. Flamant, D. Gomès, P. S. Zammit, S. Tajbakhsh, *Dev. Biol.* **2007**, *312*, 13.
[30] K. M. Wisdom, S. L. Delp, E. Kuhl, *Biomech. Model. Mechanobiol.* **2014**, *14*, 195.
[31] K. Donnelly, A. Khodabukus, A. Philp, L. Deldicque, R. G. Dennis, K. Baar, *Tissue Eng., Part C* **2010**, *16*, 711.
[32] C. A. Powell, B. L. Smiley, J. Mills, H. H. Vandenburgh, *Am. J. Physiol.: Cell Physiol.* **2002**, *283*, C1557.
[33] P. Heher, B. Maleiner, J. Prüller, A. H. Teuschl, J. Kollmitzer, X. Monforte, S. Wolbank, H. Redl, D. Rünzler, C. Fuchs, *Acta Biomater.* **2015**, *24*, 251.
[34] H. H. Vandenburgh, P. Karlisch, J. Shansky, R. Feldstein, *Am. J. Physiol.* **1991**, *260*, C475.
[35] C. Duan, H. Ren, S. Gao, *Gen. Comp. Endocrinol.* **2010**, *167*, 344.
[36] R. J. Devolder, H. Bae, J. Lee, H. Kong, *Adv. Mater.* **2011**, *23*, 3139.
[37] J. T. Finer, R. M. Simmons, J. A. Spudich, *Nature* **1994**, *368*, 113.
[38] S. Ostrovidov, V. Hosseini, S. Ahadian, T. Fujie, S. P. Parthiban, M. Ramalingam, H. Bae, H. Kaji, A. Khademhosseini, *Tissue Eng., Part B* **2013**, *20*, 403.
[39] S. Rangarajan, L. Madden, N. Bursac, *Ann. Biomed. Eng.* **2014**, *42*, 1391.
[40] G. Cittadella Vigodarzere, S. Mantero, *Front. Physiol.* **2014**, *5*, 362.
[41] K. S. Toohey, N. R. Sottos, J. A. Lewis, J. S. Moore, S. R. White, *Nat. Mater.* **2007**, *6*, 581.
[42] A. R. Hamilton, N. R. Sottos, S. R. White, *Adv. Mater.* **2010**, *22*, 5159.
[43] S. R. White, J. S. Moore, N. R. Sottos, B. P. Krull, W. A. S. Cruz, R. C. R. Gergely, *Science* **2014**, *344*, 620.
[44] D. M. Neal, M. S. Sakar, H. H. Asada, in *Am. Control Conf.*, **2013**, Whashington, DC, USA, pp. 1513–1518.
[45] R. Raman, C. Cvetkovic, R. Bashir, *Nat. Protoc.* **2017**, *12*, 519.
[46] S. G. M. Uzel, R. J. Platt, V. Subramanian, T. M. Pearl, C. J. Rowlands, V. Chan, L. A. Boyer, P. T. C. So, R. D. Kamm, *Sci. Adv.* **2015**, *2*, 1.